**Engineering Letters, 16:3, EL_16_3_16**

# Controlled Permanent Magnet Drives

C. Grabner

*Abstract* — The considered converter-fed permanent magnet motor could alternatively be operated in two basically different states – the vector control mode or alternatively the brushless dc, also known as electronically commutated mode. Several quality aspects concerning the system performance have been comparatively investigated in practical as well as theoretical manner. Focus is thereby given to the numerical analysis and previous evaluation of the well interaction between the novel axially un-skewed higher harmonic air-gap wave based permanent magnet motor design and both completely different control algorithms.

*Index Terms*—Vector control; brushless dc; electronically commutation; higher harmonic air-gap wave; drive control; finite element analysis.

## I. INTRODUCTION

A straightforward industrial development process of electrical variable speed drive systems is fortunately assisted by modern commercial calculation tools [1-3]. However, the extensive and almost precise analysis of the interaction of different control algorithms, like the vector control or the brushless DC mode, within introduced innovative permanent magnet motor topologies, as e.g. the higher harmonic air-gap based design, is still a big challenge [4-6]. Several simplifications have to be done in order to treat the analysis in a reasonable way. The implemented main software features, the interacting converter hardware and the motor itself are almost analyzed in the time-domain.

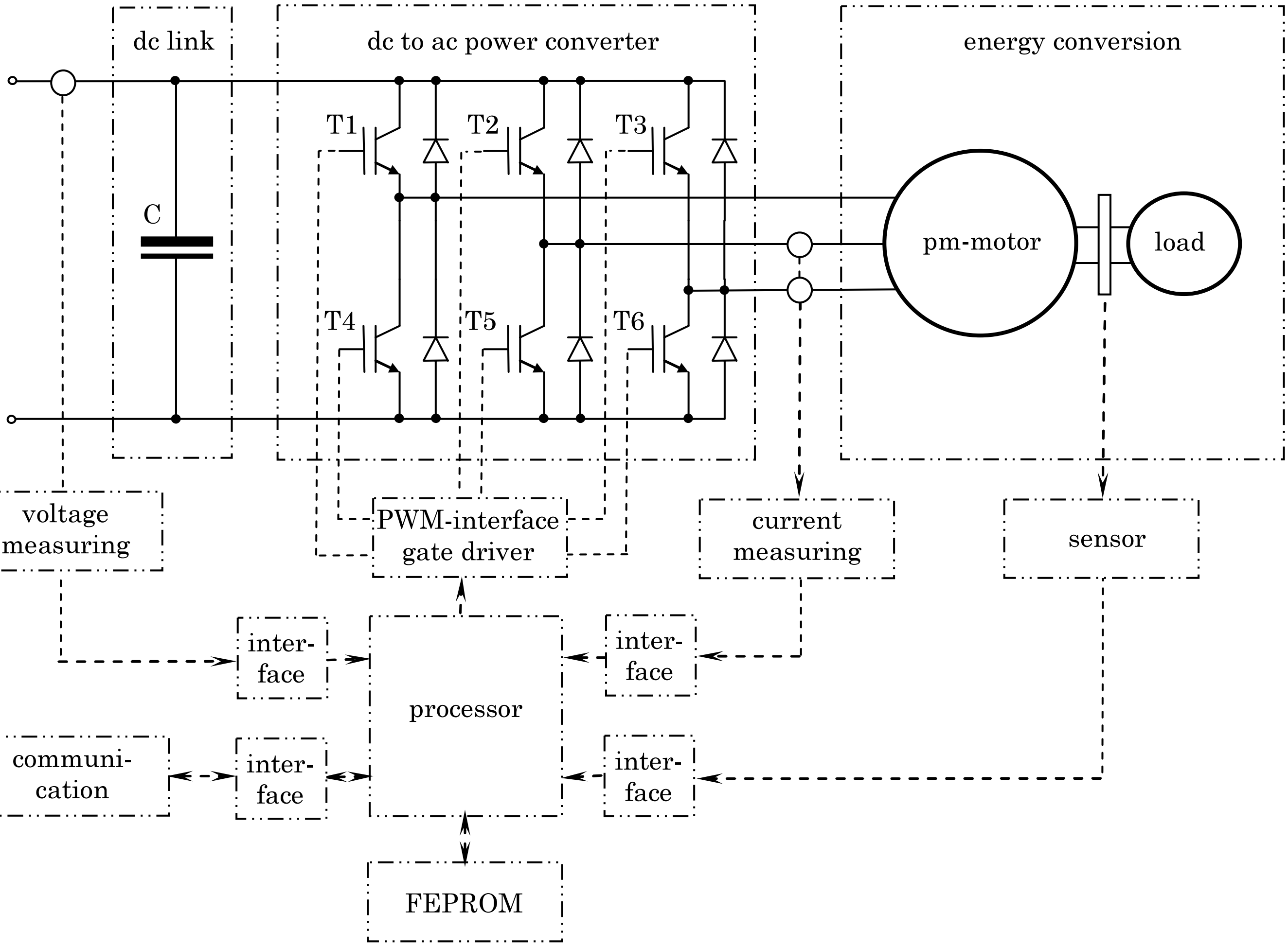

Fig.1. Outline of important devices of the considered drive system.

Manuscript received June 23, 2008.

Christian Grabner is with the Research and Development Department of Drive Systems, Siemens AG, Frauenauracherstrasse 80, D-91056 Erlangen, Germany, (phone: +49 162 2515841, e-mail: grabner.christian@siemens.com).

## II. REALIZED DRIVE SYSTEM

The investigated drive system is made up of many different hardware components [7-9]. The essential internal interaction between the supply dc-link, the dc to ac power converter, the motor, the sensor, the controllers and communicating tasks is schematically depicted in Fig.1. The realization of some constituent parts used in Fig.1 is shown in Fig.2 and Fig.3.

The power conversion from the constant dc voltage link level to the ac voltage system at the motor is elementary performed by the PWM technology.

The motor construction itself is built up for a mechanical load torque of approximately 1.35 Nm. The rotating shaft is assisted with a sensor which measures the actual position. Depending on the control mode, an encoder or Hall-sensor is used. The main current and speed control algorithm for a stable operational behavior is implemented in the 128 Kbyte flash ROM of the XC164 controller. The controller is further equipped with a 4 Kbyte RAM and has an external FEPROM memory of 512 Kbyte for other communication purposes.

Fig.2. Realized electrical power and control unit.

Fig.3. Permanent magnet assisted rotor (left) and novel stator topology with a three phase winding system (right).

## III. HIGHER HARMONIC AIR-GAP WAVE BASED PERMANENT MAGNET MOTOR DESIGN

The applied principle of synchronous energy conversion is based on the steady interaction of two separate parts — stator and rotor — of same rotational speed and a coinciding even number of alternating electromagnetic poles along the circumferential air gap between both considered parts [10].

The performed motor research is based on alternative possibilities for the generation of desired stator flux density waves within the air gap. The moving rotor with attached permanent magnets is characterized by its even number of involved magnetic poles, whereas the fixed novel stator winding design comprises the same pole number by means of higher space harmonics. The suggested un-skewed stator and rotor topology is thereby suitable to induce continuously electromechanical torque with very low ripple.

Do to the axially un-skewed lamination, only the 2D triangular finite element representation as shown in Fig.4 is necessary [1]. The rotor moves on stepwise during the transient calculation with the aid of the applied ‘band technique’ [2,3]. Thus, elements which are situated at these band domain may be deformed during motion since some of their nodes may follow the moving rotor reference frame and some the stationary stator part. These element distortions are occurring in dependency on the rotational movement. Thus, the continuous element distortion enforces a re-meshing of air-gap elements lying on the band.

Governing 3D stator end winding effects are commonly included in the 2D finite element calculation by external parameters within directly coupled electrical circuits, as shown in Fig.5. The applied voltage can be arbitrarily depending on time. This suggests coupling the output terminals of the power converter topology from Fig.1 directly with each stator phase to complete the power flow path. The actual rotor position is always accessible within the finite element calculation, so that basic control features could be implemented advantageously.

The controlled vector or brushless DC mode of the permanent magnet motor is preferable treated with numerical methods in the time-domain [3]. As a consequence, eventually occurring higher harmonics in the calculated time courses of current or torque which are succeeding limiting values could be monitored in advance. Thus, further costs for extensive prototyping could be avoided.

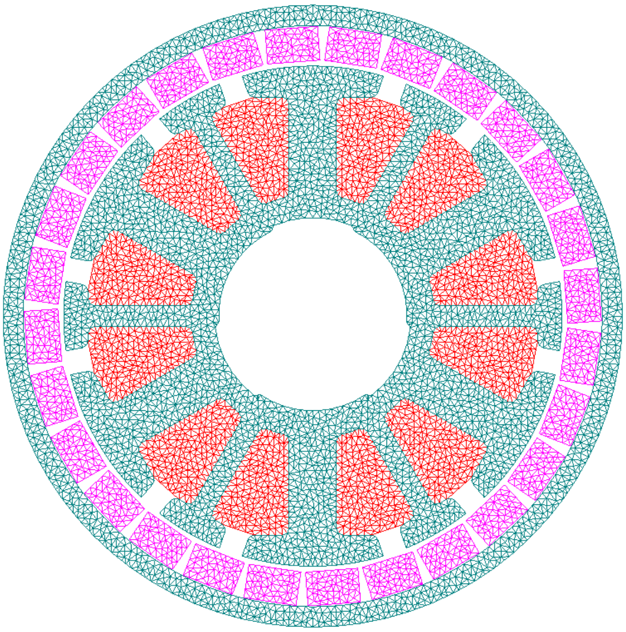

Fig.4. Finite element mesh of rotor and stator laminations, magnets, and stator winding system within the plane xy-coordinate system.

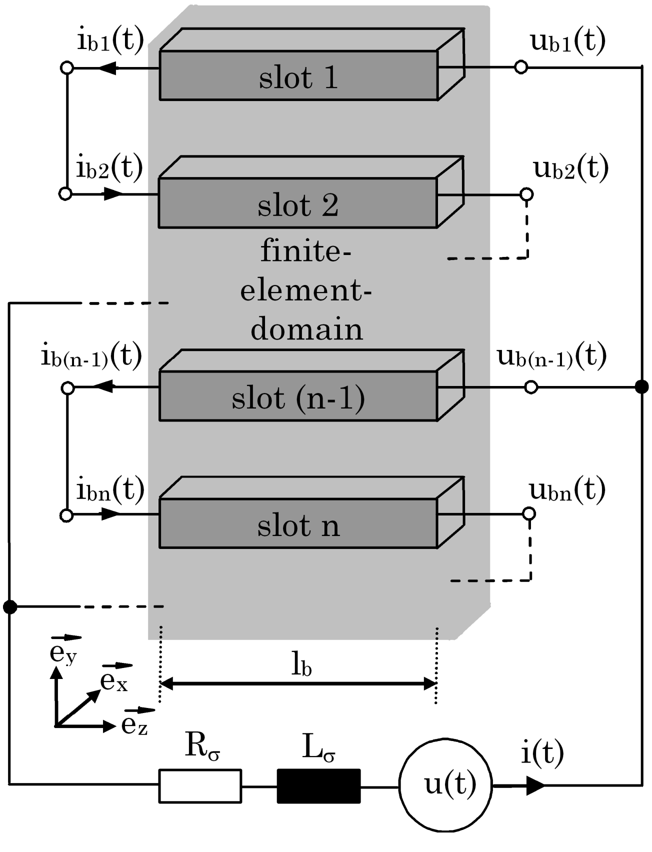

Fig.5. Coupling of the 2D finite-element-model to one stator phase circuit with external parameters which are representing 3D end winding effects.

### *A. Design of the permanent magnet rotor*

The rotor part depicted in Fig.3 has an outer bore diameter of about 46 mm and is arranged with a number of 28 single NdFeB magnets with alternating magneto-motive forces of approximately $H_c = -1 \cdot 10^6$ A/m for the rated temperature level. One magnet is 2.5 mm height and 3.9 mm wide. The magnetic remanence flux density is thereby about 1.3 T. The invoked distribution of the magnetic field as result of the permanent magnet excitation is shown in Fig.6.

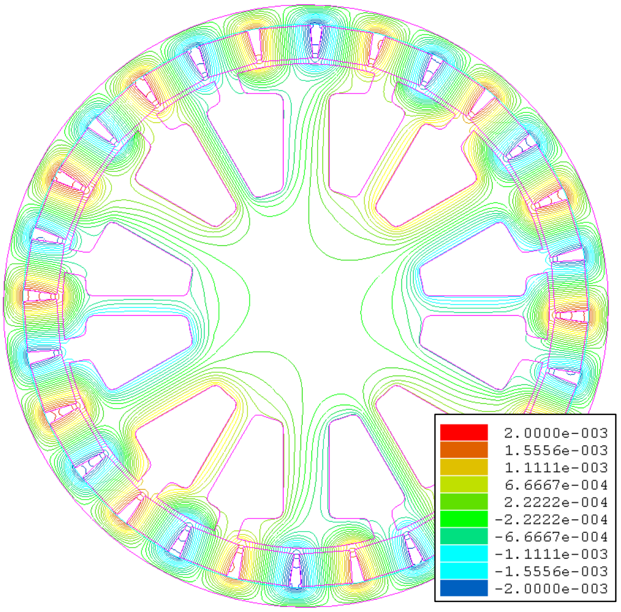

Fig.6. Magnetic vector potential lines at no-load.

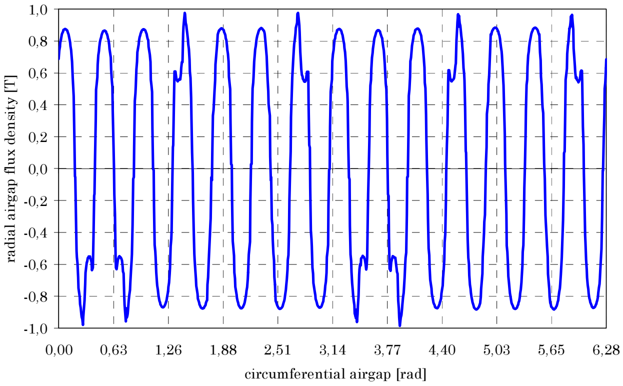

Fig.7. Calculated radial flux density component along the circumferential air gap distance at no-load.

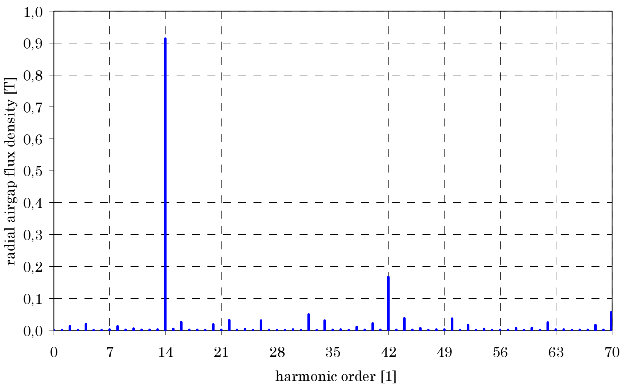

Fig.8. Fourier spectrum $\hat{B}_k$ of the radial flux density component at no-load.

Obviously a number of $p = 14$ magnetic pole pairs are generated along the circumferential air gap direction in Fig.6. Favorably, the high pole number allows a very thin yoke construction with a thickness of about only 1.5 mm. The limitation is not only caused by a restricted iron magnetic utilization in order to avoid unforeseen saturation effects and consequently losses. Also mechanical properties have to be taken into account.

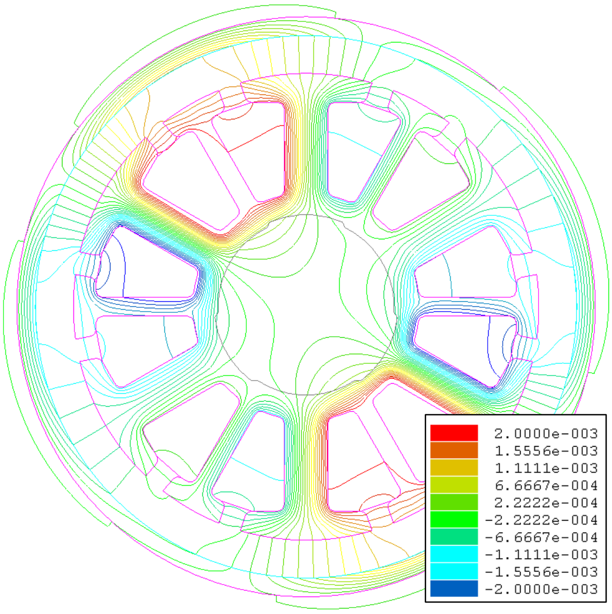

Fig.9. Magnetic vector potential lines at stator current.

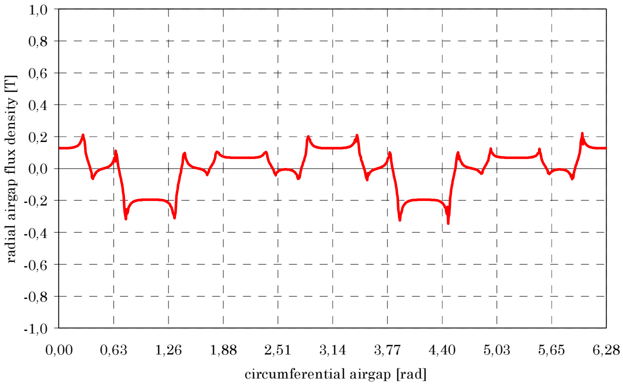

Fig.10. Calculated radial flux density component along the circumferential air gap distance at default stator current.

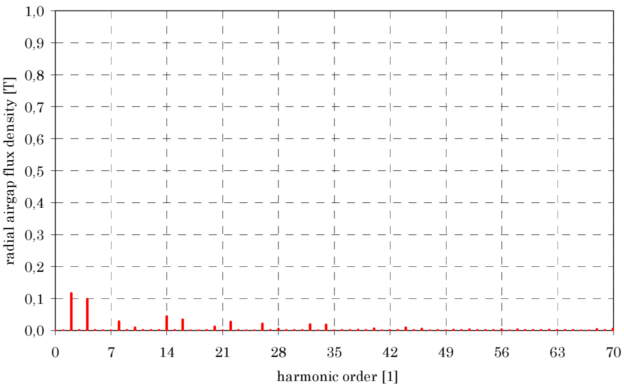

Fig.11. Fourier spectrum $\hat{B}_k$ of the radial flux density component at default stator current.

The radial flux density component $\mathrm{B_r}(\varphi)$ along the circumferential air gap distance is shown in Fig.7. The series space expansion

$$B_r(\varphi) = \sum_{k=0}^{\infty} \hat{B}_k \sin\left(k \cdot \frac{\varphi}{2\pi} + \alpha_k\right) \tag{1}$$

yields several harmonic coefficients $\hat{\mathrm{B}}_k$, $k \in \mathbb{N}$ with some very distinct contributions as it is obvious from Fig.8. The fourteenth component $\hat{\mathrm{B}}_{14} = 0.91\,\mathrm{T}$ in the no-load spectrum acts thereby as the fundamental air gap active wave of the motor.

### B. *Innovative stator design invoking higher harmonics*

In order to generate the same number of $\mathrm{p} = 14$ rotor pole pairs, a fourteenth harmonic wave in the circumferential air gap flux density distribution has to be generated from the stator current excitation. This is advantageously done by the established alternating thin and thick tooth structure along the circumferential air gap as indicated in Fig.3. For that purpose, tooth widths of approximately 1.5 mm and 3.5 mm are used.

The innovative stator winding schema presented in Fig.3 originates from a three phases winding system. Each of the necessary 12 stator slots in Fig.4 has an average slot height of 7.5 mm and a maximum slot width of 5.8 mm. The tooth winding system in Fig.5 is carried out with 43 thin wires per slot and two parallel branches. The stator part shows a bore diameter of about 37 mm and a stator yoke thickness of 2 mm. The slot width is almost 1.8 mm in order to insert the single layer winding system automatically. The shaft diameter in Fig.4 is about 14 mm.

The numerically calculated distribution of the magnetic field due to the stator current excitation only is shown in Fig.9, whereas the according radial flux density component along the circumferential air gap distance is depicted in Fig.10. From the series expansion (1), the harmonic components $\hat{\mathrm{B}}_k$, $k \in \mathbb{N}$ of the wide spectrum in Fig.11 are obtained. There exists a lot of ordinal numbers with even different magnitudes. However, only the invoked fourteenth component with $\hat{\mathrm{B}}_{14} = 0.045\,\mathrm{T}$ can interact with the rotor part in order to generate a constant mechanical average torque. Other harmonic waves are therefore undesired and cause losses. In order to restrict such effects, the geometric air gap distance is limited to be minimal of about 0.34 mm. Due to the used surface magnet design the magnetic air gap distance is wide enough to restrict additional losses within the rotor magnets due to excessively eddy current effects. This is also obviously from Fig.9 due to the very weak penetration of the stator field into the magnets and the rotor yoke.

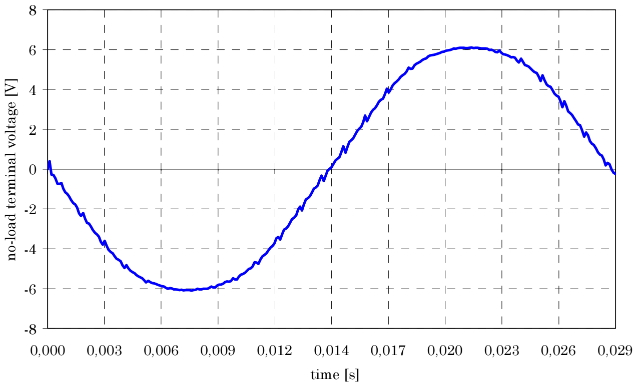

Fig.12. Calculated time-dependent phase-to-phase voltage for a constant speed of 150 rpm.

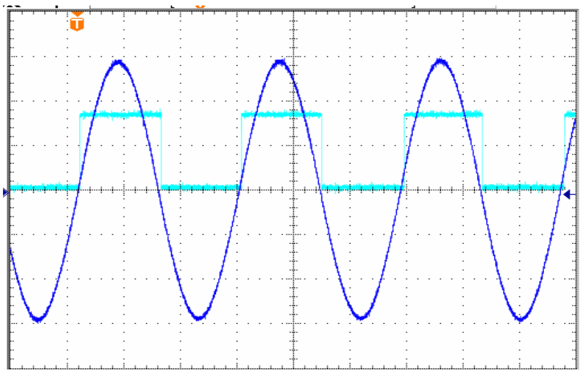

Fig.13. Measured time-dependent phase-to-phase voltage for a constant speed of 150 rpm. One division corresponds to 10 ms in the abscissa and 2 V in the ordinate.

### C. *Induced no-load voltage at constant speed*

Irregularities in the air gap caused by slots and magnetic inhomogenities in the magnetic material tend to produce higher harmonics in the induced voltage in simple winding designs [10].

The proposed un-skewed motor construction of 140 mm axial length with surface magnets and a single tooth winding system overcomes such circumstances and delivers a sinusoidal stator voltage shape as shown in Fig.12. With the number of $\mathrm{p} = 14$ poles and a constant speed of 150 rpm, the fundamental supply frequency is $\mathrm{f} = \mathrm{np} = 35\,\mathrm{Hz}$ and the relevant fundamental period is 28.6 ms. A comparison of the numerical calculated results with the measured voltage in Fig.13 shows a very good correlation.

### D. *Cogging torque effects at constant speed*

Since the demands for torque uniformity is essential, these detrimental factors must be taken into account during the machine design in order to reduce undesired cogging torque effects. Thus, negative impacts on the accuracy of the shaft's even speed or excessive acoustic noise emission could be prevented. This becomes more crucial, when un-skewed stator and rotor parts are used [10].

The calculated cogging torque at generator no-load operation in case of the un-skewed motor design in Fig.3 is exemplarily shown in Fig.14.

If the rotor is running at 10 rpm, one full rotor evolution takes 6 s. With the number of $p = 14$ poles and a constant speed of 10 rpm, the fundamental supply frequency is $f = np = 2.33\,\text{Hz}$. From Fig.14, there are 14 peaks during 1/6 of a full rotor revolution found. A comparison with the measured cogging torque at 10 rpm is presented in Fig.15. The numerical calculated spectrum in Fig.16 shows a distinct cogging torque component of 0.105 Nm at the frequency of $6f = 14\,\text{Hz}$.

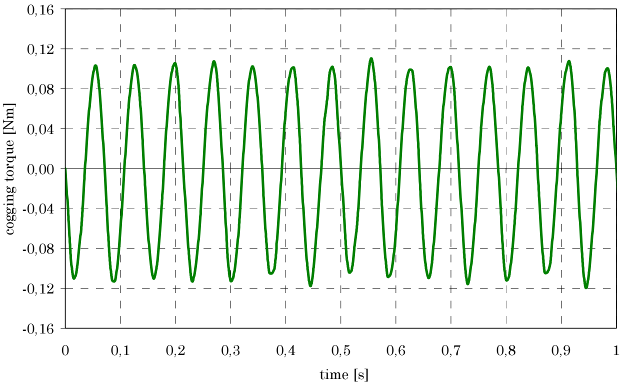

Fig.14. Calculated cogging torque for speed of 10 rpm.

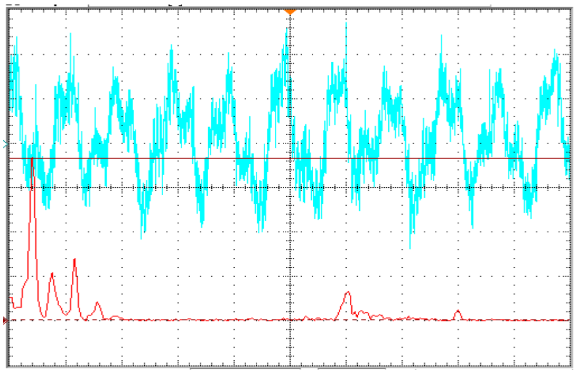

Fig.15. Measured cogging torque for a constant speed of 10 rpm. One division corresponds to 70 ms in the abscissa and 0.05 Nm in the ordinate.

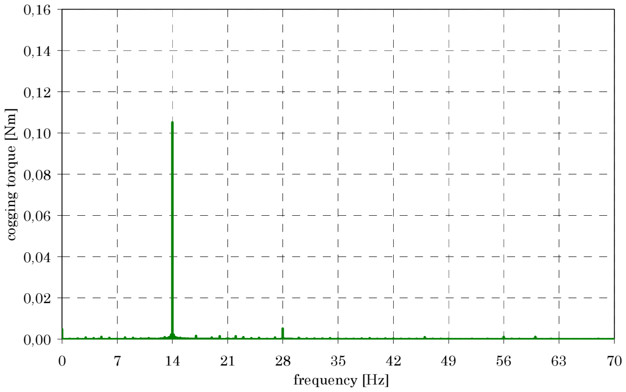

Fig.16. Fourier analysis of the cogging torque for 10 rpm.

## IV. VECTOR CONTROLLED HIGHER HARMONIC AIRGAP-WAVE BASED PERMANENT MAGNET MOTOR

The vector control mode operates the permanent magnet motor like a current source inverter driven machine applying a continuous current modulation [11-13]. Therefore, a very precise knowledge of the rotor position is necessary. This could be managed by applying an encoder on the rotating shaft. The vector control software is adapted to the hardware system which is schematically depicted in Fig.2.

### A. *Mathematical motor model*

The practical realization of the control structure is fortunately done within the rotor fixed $(d,q)$ reference system, because the electrical stator quantities can there be seen to be constant within the steady operational state [14,15]. The stator voltage and flux linkage space vectors are therefore formulated in the $(d,q)$ rotor reference frame as

$$\underset{\sim}{u}_{Sdq}(\tau) = r_S\,\underset{\sim}{i}_{Sdq}(\tau) + \frac{d\underset{\sim}{\psi}_{Sdq}(\tau)}{d\tau} + j\omega(\tau)\,\underset{\sim}{\psi}_{Sdq}\ , \tag{2}$$

$$\underset{\sim}{\psi}_{Sdq}(\tau) = l_S\,\underset{\sim}{i}_{Sdq}(\tau) + \underset{\sim}{\psi}_{Mdq}\ , \tag{3}$$

whereby $r_S$ denotes the normalized stator resistance and $\omega(\tau)$ stands for the mechanical speed of the shaft. Thereby, the relation (3) covers only weak-saturable isotropic motor designs.

The inclusion of some basic identities for the permanent magnet flux space vector in the $(d,q)$ system, namely

$$\frac{d}{d\tau}\underset{\sim}{\psi}_{Mdq} = 0\,,\ \underset{\sim}{\psi}_{Mdq} = \psi_M + j0\ , \tag{4}$$

reduces the system (2), (3) to the set of equations

$$u_{Sd}(\tau) = r_S i_{Sd}(\tau) + l_S\frac{d}{d\tau}i_{Sd}(\tau) - \omega l_S i_{Sq}(\tau)\ , \tag{5}$$

$$u_{Sq}(\tau) = r_S i_{Sq}(\tau) + l_S\frac{d}{d\tau}i_{Sq}(\tau) + \omega l_S i_{Sd}(\tau) + \omega\psi_M\ . \tag{6}$$

Unfortunately, both equations (5), (6) are always directly coupled without the exception of standstill at $\omega = 0$. That fact is very unsuitable in particular for the design of the current controller. Thus, with regard to the used vector control topology, a more favorable rewritten form of (5), (6) as

$$\begin{aligned} u_d(\tau) &= u_{Sd}(\tau) + \omega l_S i_{Sq}(\tau) = \\ &= r_S i_{Sd}(\tau) + l_S\frac{d}{d\tau}i_{Sd}(\tau) \end{aligned}\ , \tag{7}$$

$$\begin{aligned} u_q(\tau) &= u_{Sq}(\tau) - \omega l_S i_{Sd}(\tau) - \omega\psi_M = \\ &= r_S i_{Sq}(\tau) + l_S\frac{d}{d\tau}i_{Sq}(\tau) \end{aligned}\ , \tag{8}$$

is commonly introduced.

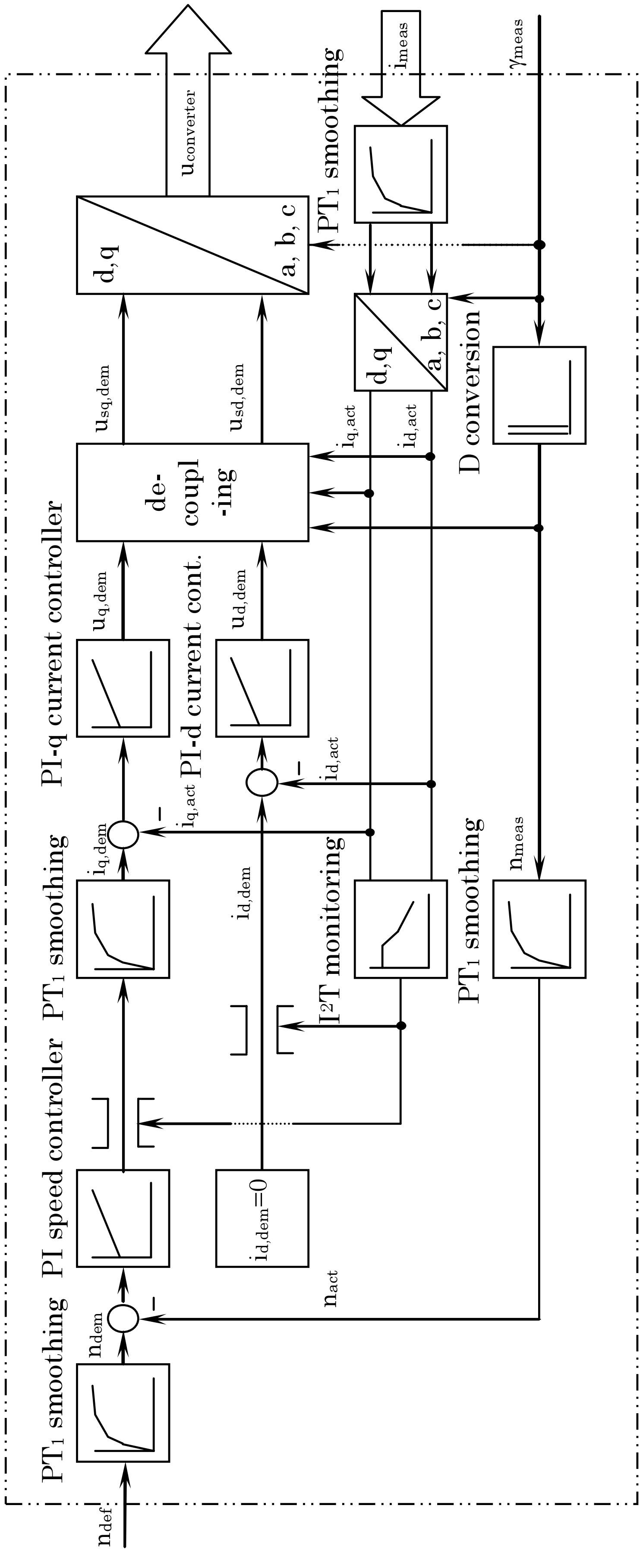

Fig.17. Outline of important devices of the vector controlled permanent magnet motor.

### *B. Simplified block diagram of the closed-loop vector control*

The control schema in accordance to (7), (8) is realized in Fig.17 separately with regard to the d- and q-axis notation as a two-step overlaid cascade structure. The outer speed cascade allows adjusting a pre-set speed value $n_{def}$, after getting smoothed by PT1 element.

The output of the PI speed controller is also smoothed by a PT1-element and restricted by the thermal $I^2t$-protection in order to avoid thermal damages. The PI speed controller has a moderate sampling rate and determines the demanded q-current component. The drive is operated with a default zero d-current component in order to achieve maximal torque output.

The actual measured electrical phase currents are transformed to the rotor fixed $(d, q)$ reference system and continuously compared to the demanded d and q current components at the innermost current cascade structure. With regard to the d- and q-axis separation, the generated PI-current controller output voltages $u_d(\tau)$, $u_q(\tau)$ are almost seen as fictive quantities in Fig.17, from which the de-coupling-circuit given in Fig.18 calculates the real demanded stator voltage components $u_{Sd}(\tau)$, $u_{Sq}(\tau)$ afterwards. The PI current controller is processed by a sampling rate of 8 kHz.

After transformation of the demanded stator voltage space vector into the $(\alpha, \beta)$ stator coordinate system, the power converter hardware generates the according voltages by using the PWM technique.

The decoupled structure (7), (8) introduces in Fig.18 fortunately both fictive voltages $u_d(\tau)$, $u_q(\tau)$ in order to adjust the controller of both axes independently from each other.

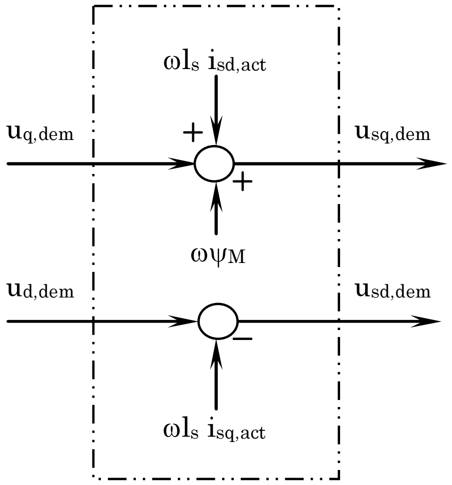

Fig.18. Block diagram of the decoupling-circuit.

### *C. Electrical current shape and harmonic spectrum*

The vector control operation within the quasi-steady operational state at rated-load condition and a default speed value of 400 rpm enforces the time dependent current shape depicted in Fig.19 within the numerical calculation. A direct comparison with the measured course in Fig.20 in real-time conditions shows a very good agreement and confirms the assumptions and simplifications within the numerical analysis procedure. The series expansion

$$i(t) = \sum_{k=1}^{\infty} \hat{I}_k \sin\left(2\pi k f \cdot t + \beta_k\right) \tag{9}$$

of the calculated electrical current from Fig.19 leads the harmonic components $\hat{I}_k$, $k \in \mathbb{N}$. It is obvious from the spectrum in Fig.21, that only the desired fundamental component $\hat{I}_1 = 3.75\text{A}$ at 93.3 Hz is governing the total spectrum. The vector control in conjunction with the special motor obviously avoids additional harmonic components and restricts therefore unexpected thermal heating due to time-harmonic currents.

### *D. Mechanical torque and harmonic spectrum*

The numerical calculated time-dependent mechanical torque m(t) is depicted in Fig.22. It results from the series expansion in time

$$m(t) = \sum_{k=0}^{\infty} \hat{M}_k \sin\left(2\pi k f \cdot t + \lambda_k\right) \tag{10}$$

that there exists within the harmonic components $\hat{M}_k$, $k \in \mathbb{N}_0$ almost the desired constant contribution of $\hat{M}_0 = 1.3\text{Nm}$. By taking a closer look to the calculated mechanical torque in Fig.23, a very distinct undesired harmonic component $\hat{M}_6 = 0.1\text{Nm}$ known as load pulsation moment exists even in spite of the novel un-skewed motor topology at the frequency of 559.8 Hz.

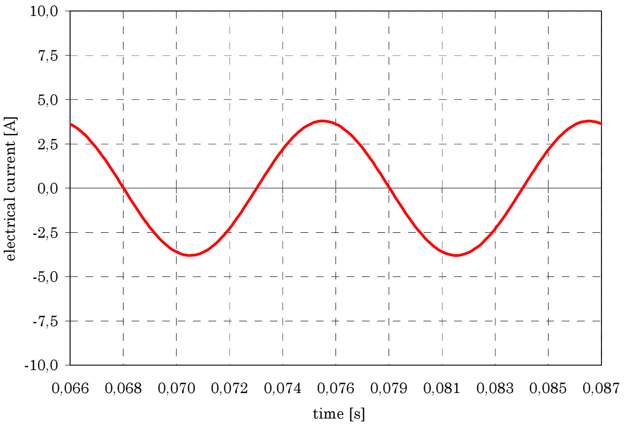

Fig.19. Calculated motor current i(t) for a speed range of 400 rpm and a constant load of 1.35 Nm.

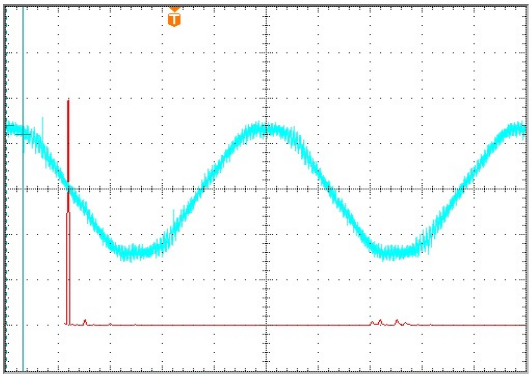

Fig.20. Measured motor current i(t) for a speed range of 400 rpm and a constant load of 1.35 Nm. One division corresponds to 2 ms in the abscissa and 2.5 A in the ordinate.

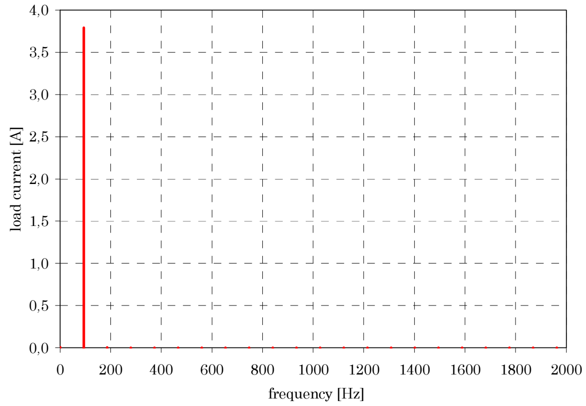

Fig.21. Fourier coefficients $\hat{I}_k$ of the motor current for a speed range of 400 rpm and a constant load of 1.35 Nm.

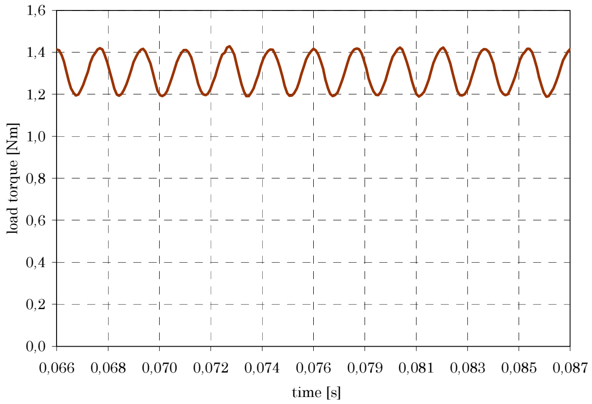

Fig.22. Calculated electromagnetic torque m(t) for a speed range of 400 rpm and a constant load of 1.35 Nm.

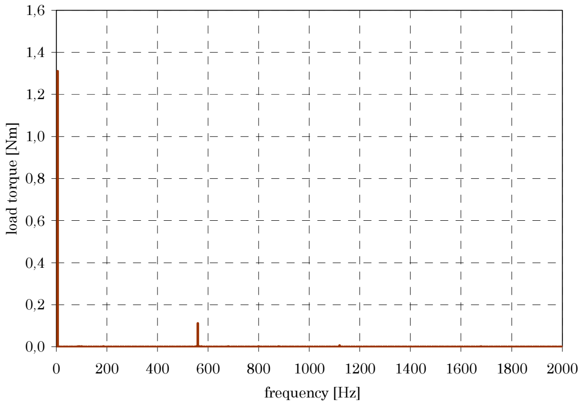

Fig.23. Fourier coefficients $\hat{M}_k$ of the shaft torque for a speed range of 400 rpm and a constant load of 1.35 Nm.

## V. Brushless DC Controlled Higher Harmonic Air-Gap Wave Based Permanent Magnet Motor

The brushless DC magnet motor is operated with a space current distribution which does not rotate smoothly but remains fixed in distinct positions within sixty electrical degrees, and then jumps suddenly to a position sixty electrical degrees ahead [16]. The brushless DC mode is also known as an electronically commutated motor operation. The current has to be commutated electronically between different phases controlled by diverse switching semiconductors [17,18]. This is possible due to three Hall sensors which provide the necessary six electrical commutation informations during the rotor shaft movement. The current magnitude is kept to a required value and the current flows only through two of the three phases coevally.

The generated average mechanical torque remains always constant within the sixty degree electrical periods. The brushless DC control algorithm is set up at the hardware system explained in Fig.2.

### A. *Mathematical motor model*

The machine equations in terms of according stator space vector notation is written in a stator fixed reference frame as

$$\underset{\sim}{u}_{S\alpha\beta}(\tau) = r_S \underset{\sim}{i}_{S\alpha\beta}(\tau) + \frac{d\underset{\sim}{\psi}_{S\alpha\beta}(\tau)}{d\tau} \quad . \tag{11}$$

The introduced stator flux space vector in (11) is fortunately written in case of weak-saturable isotropic inductances as

$$\underset{\sim}{\psi}_{S\alpha\beta}(\tau) = l_S \underset{\sim}{i}_{S\alpha\beta}(\tau) + \underset{\sim}{\psi}_{M\alpha\beta} \quad , \tag{12}$$

whereby a rotor flux space vector of constant magnitude is assumed. The governing relation for the brushless DC feature is derived from (11),(12) as

$$\underset{\sim}{u}_{S\alpha\beta}(\tau) = r_S \underset{\sim}{i}_{S\alpha\beta}(\tau) + l_S \frac{d}{d\tau} \underset{\sim}{i}_{S\alpha\beta}(\tau) + j\omega \underset{\sim}{\psi}_{M\alpha\beta} \quad , \tag{13}$$

whereby any transformation into a rotor fixed $(\mathrm{d},\mathrm{q})$ reference system is avoided.

### B. *Simplified block diagram of the closed-loop brushless DC control*

The control in Fig.24 is realized with an outer speed and an innermost current control cascade.

The imported Hall sensor signals, denoted after the interface with $\gamma_{meas}$, are transformed to a continuous actual speed value with the aid of a D-element. Due to the low number of six Hall sensors, only very rough speed detection is feasible. The smoothed signal by a PT1 is denoted as $n_{act}$. The actual speed $n_{act}$ is compared with the demanded speed $n_{dem}$. The difference is in Fig.24 applied to the moderate PI speed controller which delivers the required motor current magnitude. This value is further limited by the thermal $I^2T$ protection, which takes implicit use of the actual measured motor current $i_{act}$.

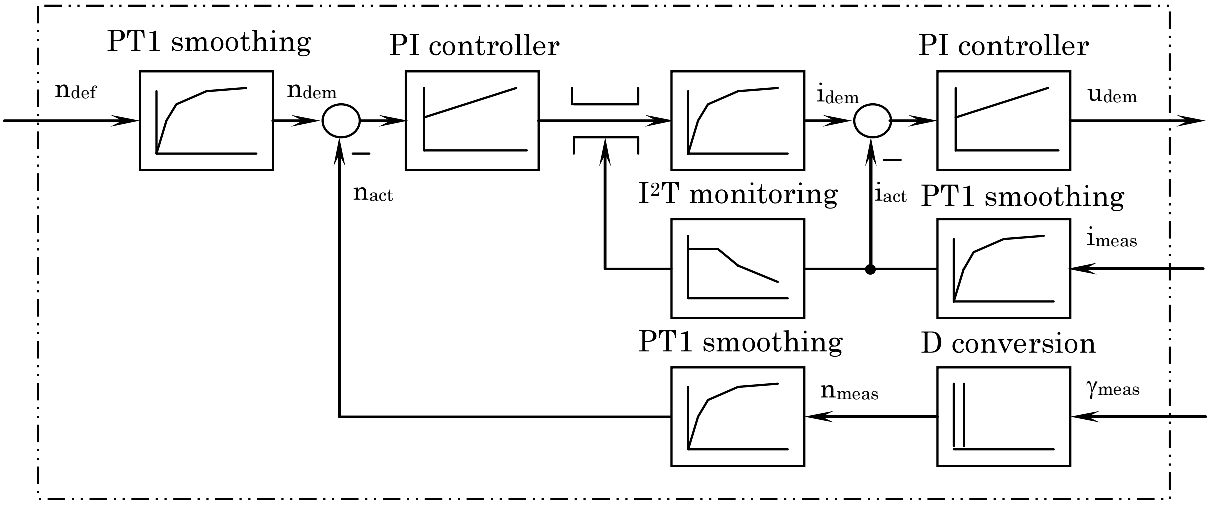

Fig.24. Simplified block diagram of the closed-loop speed and current control.

The innermost loop in Fig.24 serves as current control. The actually measured motor current $i_{meas}$ first passes a PT1 smoothing block, before the obtained signal $i_{act}$ is processed with an 8 kHz sampling rate of the current-controller. Depending on the difference between the demanded current magnitudes $i_{dem}$ and the smoothed measured current $i_{act}$, the necessary motor voltage magnitude $u_{dem}$ is calculated with the aid of a PI current controller.

### *C. Time dependent current shape and harmonic spectrum*

The influence of the electrical current commutation from one phase to the other can be clearly seen in the calculated time-dependent course of Fig.25 for rated-load and the speed of 400 rpm. The measured quantity is given in Fig.26. Direct comparison of calculated with measured courses shows a very good concordance. The implemented numerical analysis is also very suitable to predict even higher harmonics in the motor current. The complete current spectrum (9) in Fig.27 contains the fundamental component $\hat{I}_1 = 3.84\text{A}$ at 93.3 Hz. Moreover, some very distinct peaks within the spectrum could be observed. Several invoked higher harmonics such as $\hat{I}_5 = 0.81\text{A}$ at 466.6 Hz, $\hat{I}_7 = 0.62\text{A}$ at 653.3 Hz, $\hat{I}_{11} = 0.31\text{A}$ at 1026.3 Hz and $\hat{I}_{13} = 0.21\text{A}$ at 1212.9 Hz are causing negative effects, such as undesired thermal heating.

### *D. Time dependent torque and harmonic spectrum*

The numerical calculated time-dependent mechanical torque m(t) is depicted in Fig.28 for rated-load and a speed value of 400 rpm. It results from the series expansion (10) that there exists within the harmonic components $\hat{M}_k$, $k \in \mathbb{N}_0$ almost the desired constant contribution of $\hat{M}_0 = 1.36\text{Nm}$. The known undesired torque fluctuations within Fig.28 can be seen more clearly in the harmonic spectrum depicted in Fig.29. Both distinct higher components are found to be $\hat{M}_6 = 0.12\text{Nm}$ at 559.8 Hz and $\hat{M}_{12} = 0.09\text{Nm}$ at 1119.6 Hz. Other contributions to the torque ripple are obviously suppressed. The occurring undesired load tip effects are well known to be responsible for eventually undesired noise emission.

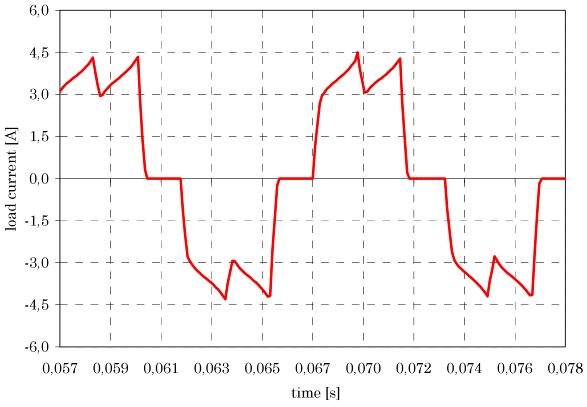

Fig.25. Calculated motor current i(t) for a speed range of 400 rpm and a constant load of 1.35 Nm.

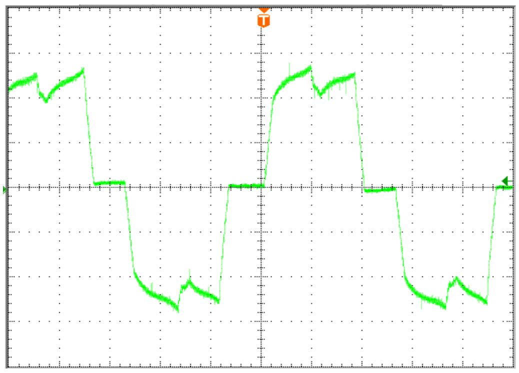

Fig.26. Measured motor current i(t) for a speed range of 400 rpm and a constant load of 1.35 Nm. One division corresponds to 2 ms in the abscissa and 1.5 A in the ordinate.

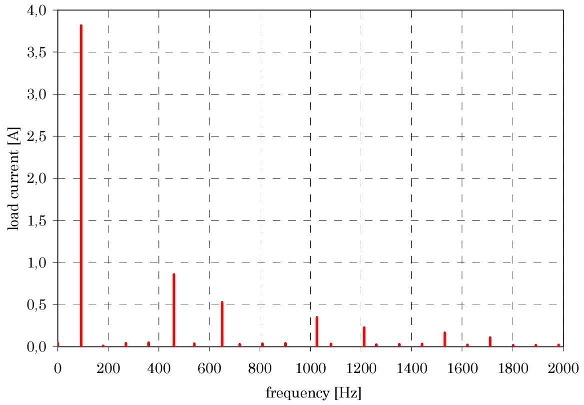

Fig.27. Fourier coefficients $\hat{I}_k$ of the motor current for a speed range of 400 rpm and a constant load of 1.35 Nm.

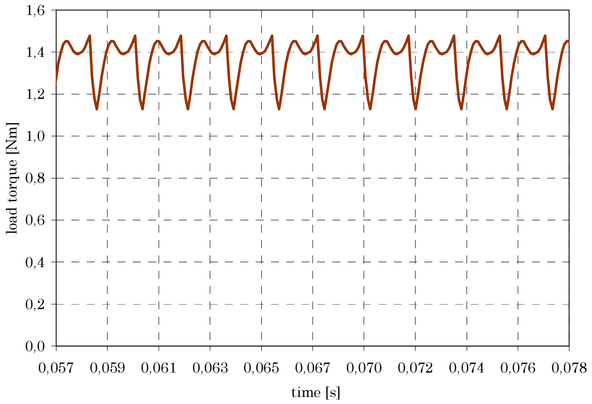

Fig.28. Calculated electromagnetic torque m(t) for a speed range of 400 rpm and a constant load of 1.35 Nm.

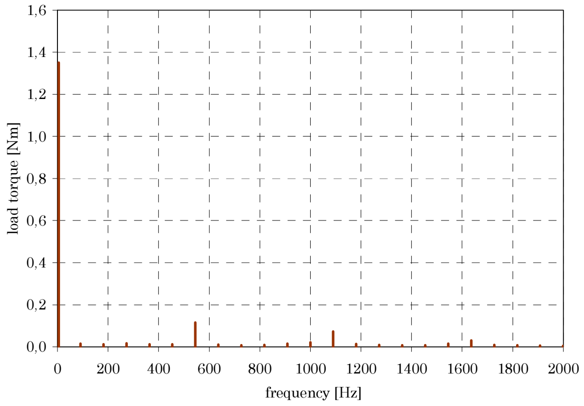

Fig.29. Fourier coefficients $\hat{M}_k$ of the shaft torque for a speed range of 400 rpm and a constant load of 1.35 Nm.

## VI. COMPARISON OF BOTH CONTROL METHODS

In case of the well-balanced motor construction and a diligent sensor adjustment, the mostly undesired torque fluctuation of the unskewed motor design still exist within the vector and brushless DC operational mode. In case of some technical applications, this disadvantage could be accepted; otherwise the rotor has to be skewed. However, for many circumstances, the easy unskewed motor construction and the much cheaper brushless DC control mode in conjunction with the higher harmonic air-gap wave based motor design is often favorized. Unfortunately, additional copper losses and varying iron losses are still reducing the thermal torque speed characteristic. In order to overcome those circumstances within certain ranges, the complex vector mode is commonly preferred.

## VII. CONCLUSION

The novel axially unskewed higher harmonic air-gap wave based permanent magnet motor technology has been analyzed with regard to the closed-loop vector as well as brushless DC control method.

The main focus is thereby given to the verification of previously unknown and almost undesired effects, which could significantly worsen the quality of the complete drive system. The vector control method enforces only one distinct fundamental component in the electrical current consumption, whereas the brushless DC control causes a wide harmonic current spectrum. Undesired load pulsation effects of the unskewed motor could be slightly reduced by preferring the vector control method.

The applied transient electromagnetic-mechanical finite element calculation method with additionally coupled external circuits in the time-domain allows the inclusion of basic control features and is therefore very suitable for a straightforward and accurate analysis of the complete converter fed speed-variable drive system in advance.

## REFERENCES

[1] J.S. Salon, *Finite element analysis of electrical machines,* Cambridge University Press: Cambridge, 1996.
[2] M.J. DeBortoli, *Extensions to the finite element method for the electromechanical analysis of electrical machines, PhD Thesis,* Rensselaer Polytechnic Institute, New York, 1992.
[3] J.P.A. Bastos and N. Sadowski, *Electromagnetic modeling by finite element method,* Marcel Dekker: New York/Basel, 2003.
[4] P.F. Brosch, *Moderne Stromrichterantriebe,* Vogel: Würzburg, 1989.
[5] W.Leonhard, *Control of electrical drives,* Springer: Berlin, 2001.
[6] G.K. Dubey, *Fundamentals of electrical drives,* Alpha Science Int.: Pangbourne, 2001.
[7] K.B. Bimal, *Power electronics and variable frequency drives: technology and applications,* IEEE Press: New York, 1996.
[8] K. Heumann, *Principles of power electronics.* Berlin: Springer Verlag, 1986.
[9] G. Seguier and G. Labrique, *Power electronic converters: dc to ac conversion.* Berlin: Springer Verlag, 1989.
[10] T. Bödefeld and H. Sequenz, *Elektrische Maschinen,* Springer: Wien/New York, 1942.
[11] P. Vas, *Vector control of AC machines,* Oxford University Press: Oxford, 1990.
[12] K.G. Bush, *Regelbare Elektroantriebe: Antriebsmethoden, Betriebssicherheit, Instandhaltung,* Verlag Pflaum: München, 1998.
[13] W. Nowotny and T.A. Lipo, *Vector control and dynamics of AC drives,* Clarendon Press: Oxford, 2000.
[14] P. Vas, *Electrical machines and drives: A space-vector theory approach,* Clarendon Press: Oxford, 1996.
[15] P. Vas, *Parameter estimation, condition monitoring, and diagnosis of electrical machines,* Clarendon Press: Oxford, 1993.
[16] R. Lehmann, *Technik der bürstenlosen Servoantriebe,* Elektronik, Vol. 21, 1989.
[17] T.J.E. Miller, *Brushless permanent magnet and reluctance motor drives,* Clarendon Press: Clarendon, 1989.
[18] J.R. Hendershot and T.J.E. Miller, *Design of brushless permanent-magnet motors,* Oxford university press: Oxford, 1994.